Asian Journal of Pharmaceutical Sciences 19 (2024) 100924

Available online at www.sciencedirect.com

ScienceDirect

journal homepage: www.elsevier.com/locate/AJPS

Research Article

A PET probe targeting polyamine transport system for precise tumor diagnosis and therapy

Ming Zhou [a,b,1], *Xiaoqin Yin* [a,b,1], *Bei Chen* [a], *Shuo Hu* [a,c,d,*], *Wenhu Zhou* [b,d,*]

[a] *Department of Nuclear Medicine, Xiangya Hospital, Central South University, Changsha 410008, China*
[b] *Xiangya School of Pharmaceutical Sciences, Central South University, Changsha 410013, China*
[c] *Key Laboratory of Biological Nanotechnology of National Health Commission, Changsha 410008, China*
[d] *National Clinical Research Center for Geriatric Disorders (Xiangya), Changsha 410008, China*

ARTICLE INFO

Article history:
Received 25 December 2023
Revised 2 February 2024
Accepted 4 March 2024
Available online 25 April 2024

Keywords:
PET imaging
Polyamine metabolism
Spermine
Radiopharmaceutical
Melanoma

ABSTRACT

Polyamine metabolism dysregulation is a hallmark of many cancers, offering a promising avenue for early tumor theranostics. This study presents the development of a nuclear probe derived from spermidine (SPM) for dual-purpose tumor PET imaging and internal radiation therapy. The probe, radiolabeled with either [^{68}Ga]Ga for diagnostic applications or [^{177}Lu]Lu for therapeutic use, was synthesized with exceptional purity, stability, and specific activity. Extensive testing involving 12 different tumor cell lines revealed remarkable specificity towards B16 melanoma cells, showcasing outstanding tumor localization and target-to-non-target ratio. Mechanistic investigations employing polyamines, non-labeled precursor, and polyamine transport system (PTS) inhibitor, consistently affirmed the probe's targetability through recognition of the PTS. Notably, while previous reports indicated PTS upregulation in various tumor types for targeted therapy, this study observed no positive signals, highlighting a concentration-dependent discrepancy between targeting for therapy and diagnosis. Furthermore, when labeled with [^{177}Lu], the probe demonstrated its therapeutic potential by effectively controlling tumor growth and extending mouse survival. Investigations into biodistribution, excretion, and biosafety in healthy humans laid a robust foundation for clinical translation. This study introduces a versatile SPM-based nuclear probe with applications in precise tumor theranostics, offering promising prospects for clinical implementation.

* Corresponding authors at: Xiangya School of Pharmaceutical Sciences, Central South University, Changsha 410013, China.
E-mail addresses: hushuo2018@163.com (S. Hu), zhouwenhuyaoji@163.com (W. Zhou).

1 These authors contributed equally to this work.

Peer review under responsibility of Shenyang Pharmaceutical University.

https://doi.org/10.1016/j.ajps.2024.100924

1. Introduction

Cancer remains a formidable global health challenge, necessitating effective diagnostic and treatment strategies [1,2]. Timely diagnosis of tumors is pivotal for patient survival and improved overall outcomes. Early tumor detection hinges on the utilization of tumor-specific markers to construct corresponding recognition probes, enabling the generation of detection signals. Among clinical diagnostic methods, positron emission tomography/computed tomography (PET/CT) or positron emission tomography/magnetic resonance (PET/MR) holds unparalleled efficacy, providing insight into disease-related molecular and metabolic alterations alongside comprehensive anatomical imagery in a single session [3–5]. It is a sensitive, repeatable, and non-invasive tool extensively employed for diagnosing, staging, monitoring treatment responses, and prognosticating various cancers. It serves as a crucial step in clinical decision-making for patients with diverse malignancies. Therefore, the development of PET probes for early tumor diagnosis, characterized by high sensitivity, safety, favorable physicochemical attributes, and *in vivo* kinetic profiles, holds profound clinical significance.

In light of the metabolic disparities between cancer cells and their normal counterparts, various PET molecular probes have been designed to target biologically active small molecules exhibiting heightened uptake during tumor metabolism. For instance, [^{18}F]FLT, a thymidine analogue, offers insights into cell proliferation, primarily used in diagnosing lung and central nervous system tumors [6,7]. Amino acid PET/CT tracers such as [^{18}F]FET and [^{11}C]methionine, which gauge amino acid uptake and protein synthesis, are essential for central nervous system tumor diagnosis [8–10]. [^{11}C]choline, instrumental in membrane metabolism, serves early detection in prostate cancer and gliomas [11]. Widely employed, [^{18}F]FDG leverages abnormal glucose metabolism for imaging, albeit without tumor specificity, limited applicability to low glucose metabolism tumors, and vulnerability to confounding factors like infection or inflammation [12–15]. Furthermore, [^{18}F]FDG PET/CT is influenced by patients' blood glucose levels and ambient temperatures, necessitating fasting, which poses challenges, especially to diabetic patients [16–19]. Thus, enhancing tumor imaging via superior PET/CT probes targeting metabolic aberrations remains a pressing need.

Polyamines, including putrescine, spermidine, and spermine, play critical roles in normal cell growth and participate in various physiological processes [20–25]. Tumor cells exhibit significantly heightened polyamine metabolism compared to normal cells [26,27]. Oncogenes like MYC, RAS, and BRAFV600E stimulate polyamine biosynthesis and increase polyamine uptake through the polyamine transport system (PTS) [28–31]. Elevated polyamine levels in tumors are linked to immune suppression, rendering cancer cells sensitive to polyamine depletion [32–34]. Consequently, the FDA approved alpha-difluoromethylornithine (DFMO) as a drug targeting the rate-limiting enzyme ornithine decarboxylase (ODC) in polyamine biosynthesis [26]. However, clinical applications of DFMO face limitations due to compensatory PTS upregulation. Hence, researchers explore polyamine blockade therapy (PBT), combining polyamine synthesis inhibitors like DFMO with polyamine transport inhibitors (PTIs) in high-PTS-expressing tumor cells [34–38]. PBT not only reduces polyamine levels but also inhibits tumor growth and metastasis, and enhances the efficacy of immune checkpoint inhibitors (ICIs) [34,39]. Surprisingly, limited research focuses on polyamine-based tumor diagnostics, primarily due to the dearth of biochemical data on mammalian PTS [40–42]. Consequently, designing polyamine probes targeting specific tumors is challenging. A singular study synthesized the [^{99m}Tc]Tc-HYNIC-spermine probe for PTS SPECT imaging in B16 subcutaneous tumors [42]. However, SPECT's relatively lower spatial resolution potentially misses smaller lesions, and the cumbersome synthesis of [^{99m}Tc]Tc-HYNIC-spermine impedes its clinical utility [43].

This study introduces a novel PET/CT probe, [^{68}Ga]Ga-spermine ([^{68}Ga]Ga-SPM), targeting the PTS (Scheme 1). The probe, synthesized using spermine (SPM) as a recognition molecule and NOTA as a chelating functional group, offers rapid synthesis, high radiochemical purity, and *in vivo* and *in vitro* stability. *In vitro* cellular experiments and *in vivo* animal data involving 12 tumor cell types demonstrate [^{68}Ga]Ga-SPM's specific identification of melanoma B16 cells and their tumor-bearing mice, mediated by PTS. Notably, [^{68}Ga]Ga-SPM remains unaffected by temperature, immune microenvironment, and diet, and exhibits superior tissue specificity and signal-to-noise ratio compared to [^{18}F]FDG. Subsequently, [^{68}Ga]Ga-SPM was substituted with [^{177}Lu] for therapeutic nuclear probe development, with *in vivo* efficacy verification. Lastly, human-level investigations elucidated the probe's tissue distribution, metabolism, and safety, facilitating clinical translation. This work presents [^{68}Ga]Ga-SPM as a promising tumor probe for non-invasive, accurate diagnosis of high-PTS-expressing tumors, offering monitoring capabilities for detecting abnormal polyamine metabolism. It also provides insights into PTS expression variation in tumor cells, guiding PBT treatments more accurately (Scheme 1).

2. Material and methods

2.1. Materials

All chemicals and solvents were purchased commercially and used without further purification. Spermine, benzyl carbonochloridate (CbzCl), K_2CO_3, Pd/C, anhydrous aluminium chloride ($AlCl_3$) and sodium acetate were purchased from Energy Chemical (Shanghai, China) as reagents. NOTA-NHS and spermine were purchased from GL Biochem Co., Ltd. (Shanghai, China) as reactive materials. $^{68}GaCl_3$ (ITM 68Ge/68Ga generator, Germany) was used as a radionuclide for radiolabelling. NaOAc solution (pH = 4.0) was used as a buffer to regulate pH for radiolabelling. The radioanalysis was performed using Agilent 1260 Infinity II HPLC (Palo Alto,USA) with a Bioscan flow-count radioactivity detector and a Ultimate HILIC Amide (5 µm 4.6 × 150 mm). The radioactivity was detected with a WIZARD 2480 γ-counter (PerkinElmer, USA). Micro-PET imaging was performed on

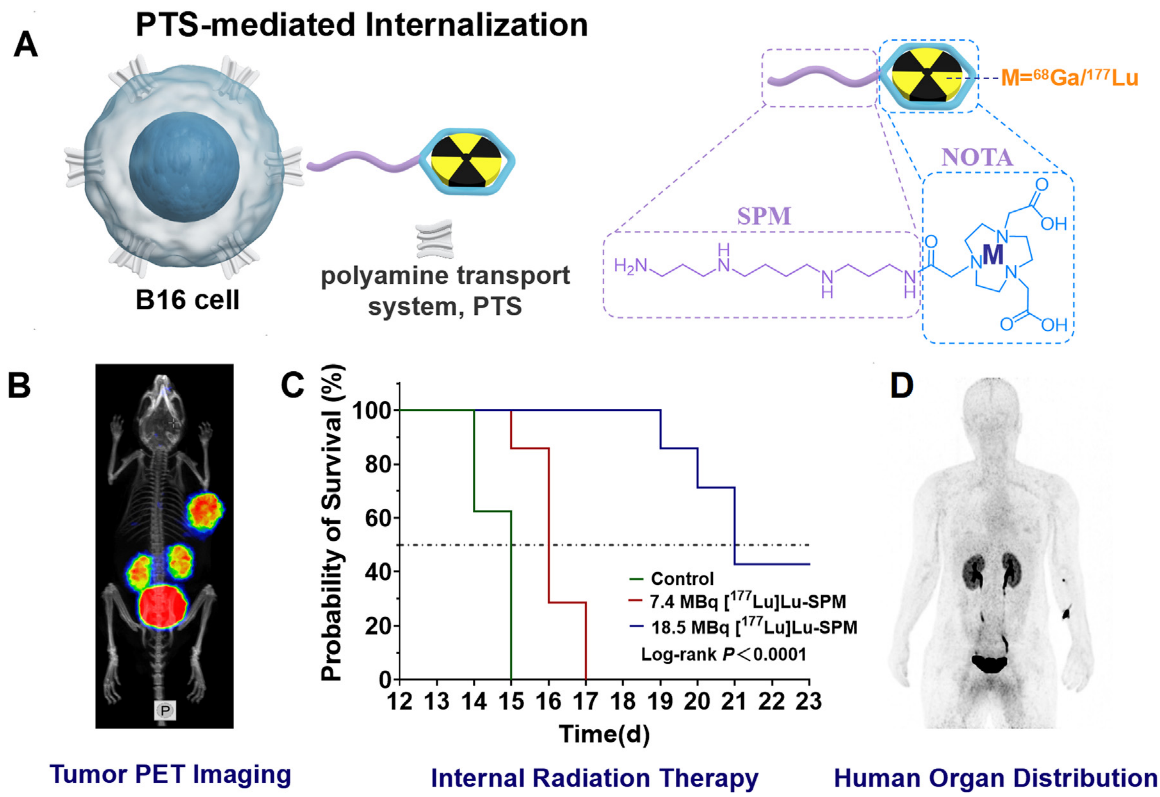

Scheme 1 – (A) The structure of the PET/CT probe and its specific internalization into tumor cell via PTS. Application of the probe in diagnosis (B) and radionuclide therapy (C) of B16 melanoma. (D) PET/CT imaging of the probe in the human body.

an Inveon PET scanner (Siemens, Germany). Human PET/CT imaging was obtained from the GE Discovery PET/CT 690 Elite scanner (Waukesha, USA) equipped with GE AW 4.6 workstation for image analysis.

2.2. *Production of NOTA-SPM and [^{177}Lu]Lu/[^{68}Ga]Ga-SPM*

NOTA-SPM was synthesized in three steps from spermine and benzyl chloroformate (CbzCl). The final product, NOTA-SPM, was fully characterized by mass spectrometry and ^{1}H NMR. The synthesis of [^{177}Lu]Lu/[^{68}Ga]Ga-labeled NOTA-spermine was detailed in supplementary materials. The final product of [^{177}Lu]Lu/[^{68}Ga]Ga-SPM was obtained from a semipreparative HPLC purification (SI).

2.3. *In vitro and in vivo stability*

For *in vitro* stability, 0.3 ml (37–45 MBq/ml) of [^{68}Ga]Ga-SPM was added to 1 ml of normal saline and human serum, and incubated at 37 °C for 0.5 h, 1 h, 2 h and 4 h, then the radiochemical purity of [^{177}Lu]Lu/[^{68}Ga]Ga-SPM was obtained by high-performance liquid chromatography (HPLC)analysis. For *in vivo* metabolic stability, blood and urine were collected from normal C57BL/6 mice after tail vein injection of [^{68}Ga]Ga-SPM (37–55.5 MBq) 1 h later. Blood was centrifuged to take supernatant, added with an appropriate amount of acetonitrile for purification, and centrifuged again. The urine was also added with acetonitrile for purification. Finally, the urine and blood samples were analyzed by HPLC.

2.4. *Cell culture*

A549, MC38, CT26, HCT116 and PC-3 cells were purchased from the Biological Cell Room, Center for Advanced Studies, Central South University, China. A375, Yummer1.7, B16/F10 (B16) and SK-MEL-28 cells were provided friendly by the Skin Research Center, Xiangya Hospital, Central South University, China. SK-MEL-3, HEK293, HL-60 and SKOV3 cells were purchased from Cobioer Biosciences Co., Ltd. and Wuhan Punosai Life Technology Co., Ltd., respectively. All cells were cultured in the corresponding medium supplemented with 10% fetal bovine serum (Corning) and 1% penicillin-streptomycin solution (Biosharp), and were grown at 37 °C and 5% CO_2.

2.5. *Cytotoxicity experiment (CCK-8 assay)*

The cell viability of A549, B16 and HEK293 upon exposure to precursor (NOTA-SPM) with concentration gradients ranging from 0 to 200 µg/ml was tested by Cell Counting Kit-8 (CCK-8) assay. Cells were incubated at 37 °C, 5% CO_2 for 24 h after adding precursor, then 10 µl CCK-8 solution was added to each well and cultured for another 2 h. In the end, the optical density (OD) value of cells at 450 nm was measured with microplate reader (Epoch, BioTek, USA). The anti-tumor effects of [^{177}Lu]Lu-SPM on B16 cells were tested by the same method. Results were analyzed using the *t*-test on Graph Pad Prism (version 9).

2.6. Cell uptake and blocking assay

A hundred µl radioactive solution containing 3.7 KBq [^{68}Ga]Ga-SPM was added to 12 kinds of tumor cells inoculated in 24-well plates 1 d in advance. The culture medium was sucked off after 15 min, 30 min, 1 h and 2 h, respectively, and washed twice with 0.5 ml ice phosphate-buffered saline (PBS) containing 0.2% bovine serum albumin (BSA). Then, cells were digested by pancreatic enzyme and collected for γ count on a γ-counter (PerkinElmer, USA). In the end, the cell count of each kind of tumor cell in each well was counted separately. Each type of cell had 4 duplicate wells at each time point; results were counted as mean ± standard deviation (SD) to express the percentage of total activity per 10^5 cells (%/10^5 cell).

B16 tumor cells (5×10^5 per well) were inoculated in 24-well plate 24 h ago and different blocking agents, including precursors NOTA-SPM, spermine, spermidine, putrescine and AMXT-1501 (inhibitor of PTS), were co-incubated with cells 1 h before the addition of radiopharmaceuticals. Then, 3.7 KBq [^{68}Ga]Ga-SPM were added according to the above method for uptake experiments.

2.7. Xenograft models

C57BL/6 and BALB/c nude mice were obtained and fostered in the Department of Zoology, Central South University, China. All animal experiments were conducted under the guidance of the Animal Care Committee of Central South University. A549, SKOV3, A375, SK-MEL-28, SK-MEL-3, HL-60, PC-3 and HCT116 cells ($1–5 \times 10^7$, 150 µl in PBS) were inoculated subcutaneously on the right shoulder of BALB/c mice (male, 5–6 weeks). Yummer1.7, B16, SK-MEL-3, MC38 and CT26 cells ($2–5 \times 10^6$, 150 µl in PBS) were inoculated subcutaneously on the right shoulder of C57BL/6 mice (male, 5–6 weeks). When the average tumor volume reached 100–150 mm^3, subsequent *in vivo* and *in vitro* experiments were conducted.

2.8. In vivo distribution studies

Twenty B16 xenograft models were injected with [^{68}Ga]Ga-SPM (1.85 MBq, 160 µl) through the tail vein, four of which were injected with 1 mg NOTA-SPM 1 h ahead of schedule, then, four mice were sacrificed and dissected at a fixed time point (0.5 h, 1 h, 2 h and 4 h) after the injection. The tissues/organs of interest were weighed and γ counted to calculate the percentage of injected dose per gram (%ID/g) and expressed as mean ± SD. By the same method, 1.11 MBq [^{177}Lu]Lu-SPM was injected into 20 B16 xenograft models and treated at 1 h, 4 h, 24 h, 48 h and 72 h to obtain %ID/g of interested tissues/organs.

2.9. In vivo micro-PET/CT imaging

Dynamic micro-PET/CT imaging was conducted under anesthesia of isoflurane/O_2 in the Inveon PET scanner (Siemens, Germany) after xenograft models injection with about 7.4 MBq (160 µl, 0.13 nmol) [^{68}Ga]Ga-SPM immediately for 60 min, then a 10-min static micro-PET/CT scan were acquired at 2 h, 3 h and 4 h after intravenous injection. The pure static micro-PET/CT imaging was performed after 30 min intravenous injection of approximately 5.55 MBq (140 µl, 0.10 nmol) [^{68}Ga]Ga-SPM or 4.44 MBq (140 µl, 0.13 nmol) [^{18}F]DMPY2 (synthesis in SI) [44]. For the [^{18}F]FDG micro-PET/CT, mice needed to fast for at least 4–6 h before injecting with 5.55 MBq (140 µl, 0.2 nmol) [^{18}F]FDG.

In blocking studies, xenograft models were injected with one of the blockers (precursor NOTA-SPM, spermine, spermidine, putrescine or AMXT-1501 2 mg/kg) 1 h in advance, then imaged according to the above methods. All images were reconstructed and analyzed in InterView^{TM} FUSION software (Mediso, HU) to obtain the%ID/g of the region of interest (ROI).

2.10. Therapy and efficacy assessment study

C57BL/6 mice (male, 5–6 weeks) were randomly assigned to three groups ($n = 7/8$) and 2×10^6 B16 cells (150 µl in PBS) were inoculated subcutaneously on their right shoulder at Day 0. When the black subcutaneous tumor could be seen on Day 3, PBS, 7.4 MBq or 18.5 MBq [^{177}Lu]Lu-SPM were injected intravenously into three groups, respectively, and the administration was repeated 3 d later (Fig. 6B). The weight and tumor volume of mice were monitored every other d, then daily monitoring was carried out when the tumor grew rapidly in the late stage. The formula for calculating tumor volume was $V = 0.5 \times (L \times M^2)$, where L represented the long diameter of the tumor and M was the minor diameter perpendicular to the long axis. The endpoint of the experiment was set as a tumor size of 1500 mm^3 or a weight loss of more than 20%. Mice that reached the destination were euthanized, and their tumors, hearts, lives, spleens, lungs, and kidneys were collected in 4% formalin for subsequent study.

2.11. Hematoxylin eosin (HE) staining

In order to evaluate the potential side effects associated with radiation exposure, we compared the HE staining of heart, liver, spleen, lungs, and kidney tissues in radionuclide treatment groups with PBS group to confirm whether there were early pathological changes. The fixed tissues were dewaxed and hydrated after paraffin embedding and section. Then, it was stained with hematoxylin staining solution for 5 min. After differentiation with hydrochloric acid, alcohol, and ammonia water returning to blue, it was dehydrated and stained with eosin for 5 min. Finally, it was transparent and sealed, then observed under a microscope (ZEISS, DE). Four 2 mm^2 areas were randomly selected in the section under 200 × magnification and determined blindly by two pathologists whether the tissue was damaged.

2.12. [^{68}Ga]Ga-SPM PET/CT imaging in healthy volunteers

The first-in-human study of [^{68}Ga]Ga-SPM was approved by the Medical Ethics Committee of Xiangya Hospital of Central South University (No.202104001). The volunteers

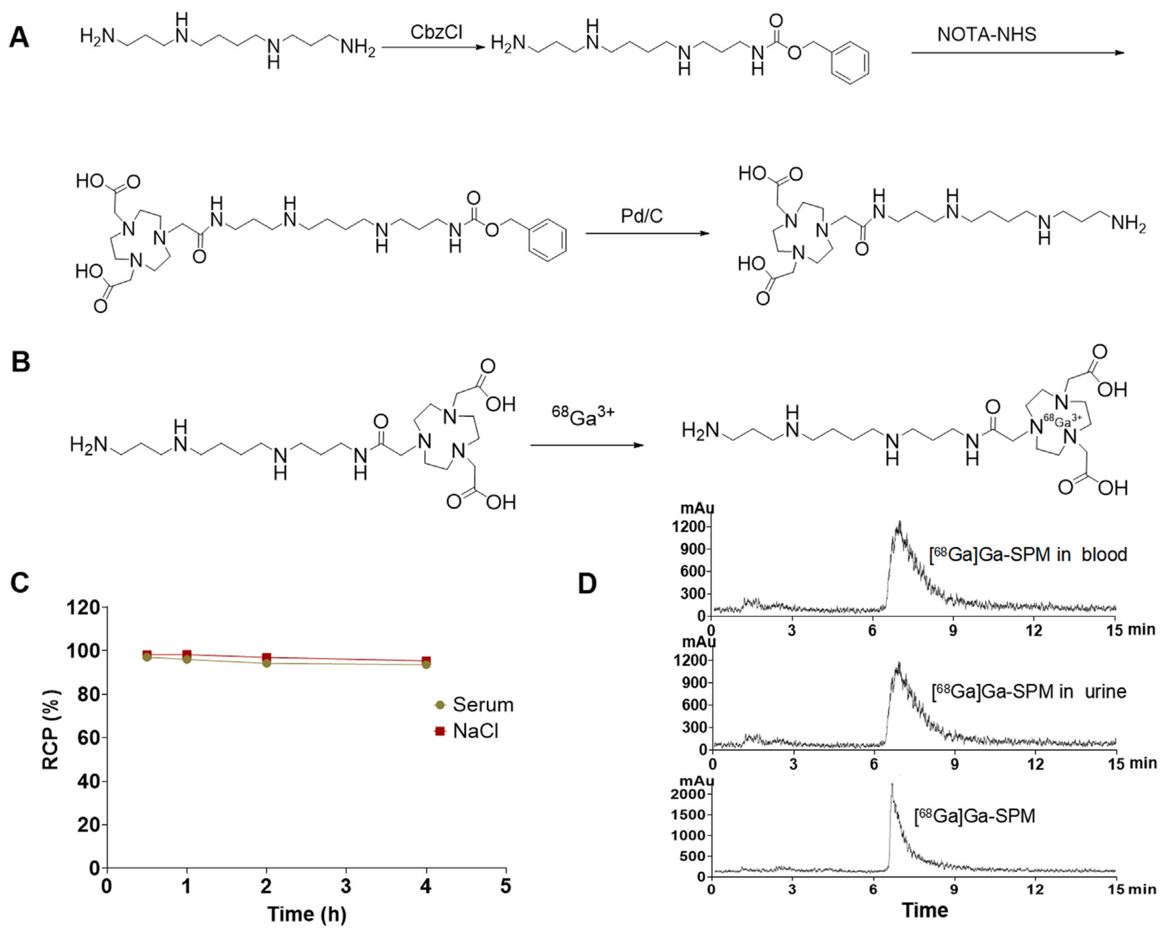

Fig. 1 – Preparation and characterizations of [^{68}Ga]Ga-SPM. (A) The synthesis of NOTA-SPM. (B) Radiosynthesis of [^{68}Ga]Ga-SPM. (C) *In vitro* stability of [^{68}Ga]Ga-SPM in normal saline and serum. (D) *In vivo* stability of [^{68}Ga]Ga-SPM in the blood and urine of normal C57BL/6 mice.

signed a written informed consent. A whole-body dynamic PET/CT imaging for 60 min was obtained immediately after injection of [^{68}Ga]Ga-SPM (3.7 MBq/kg) on a GE Discovery PET/CT 690 Elite scanner. Then, images were reconstructed with a GE AW 4.6 workstation. The maximum standardized uptake value (SUV_{max}) and mean standardized uptake value (SUV_{mean}) were measured on the volumes of interest (VOIs). The radiation dosimetry of normal volunteers was calculated by Organ Level Internal Dose Assessment Code (OLINDA, Vanderbilt University, Version 2.2) software.

2.13. *Statistical analysis*

All figures and statistical analysis were performed in GraphPad Prism 9.0 software. Quantitative data were expressed as mean ± SD. The differences between groups were compared by T-test, one-way ANOVA or Two-way ANOVA test, according to the situation. The Kaplan–Meier curve was used to evaluate the survival of mice. $P < 0.05$ was considered statistically significant, in which * represent $P \le 0.05$, ** ≤ 0.01, *** ≤ 0.001, and **** ≤ 0.0001.

3. Results and discussion

3.1. *Synthesis and characterization of [^{68}Ga]Ga-SPM*

The precursor compound NOTA-SPM was synthesized through a three-step chemical procedure encompassing protection, coupling, and deprotection reactions (Fig. 1A). The structural integrity of NOTA-SPM was confirmed via ^{1}H NMR and mass spectra, as illustrated in Figs. S1 and S2. The overall yield achieved for this synthesis was 0.73%. The radiolabeling process for [^{68}Ga]Ga-SPM, depicted in Fig. 1B, yielded a labeling efficiency of 65.4% ± 8.2%, coupled with a radiochemical purity exceeding 95%. Stability assessment serves as a pivotal criterion in evaluating the performance of radiopharmaceuticals. In this regard, we conducted an extensive investigation into the *in vitro* stability of [^{68}Ga]Ga-SPM in both saline and serum solutions. Our findings consistently demonstrated that the radiochemical purity of [^{68}Ga]Ga-SPM remained consistently above 95% after a 4-h incubation period in both media (Fig. 1C). The radiochemical purity of [^{177}Lu]Lu-SPM was performed by radio-TLC (Fig. S4). Subsequently, we administered [^{68}Ga]Ga-SPM intravenously

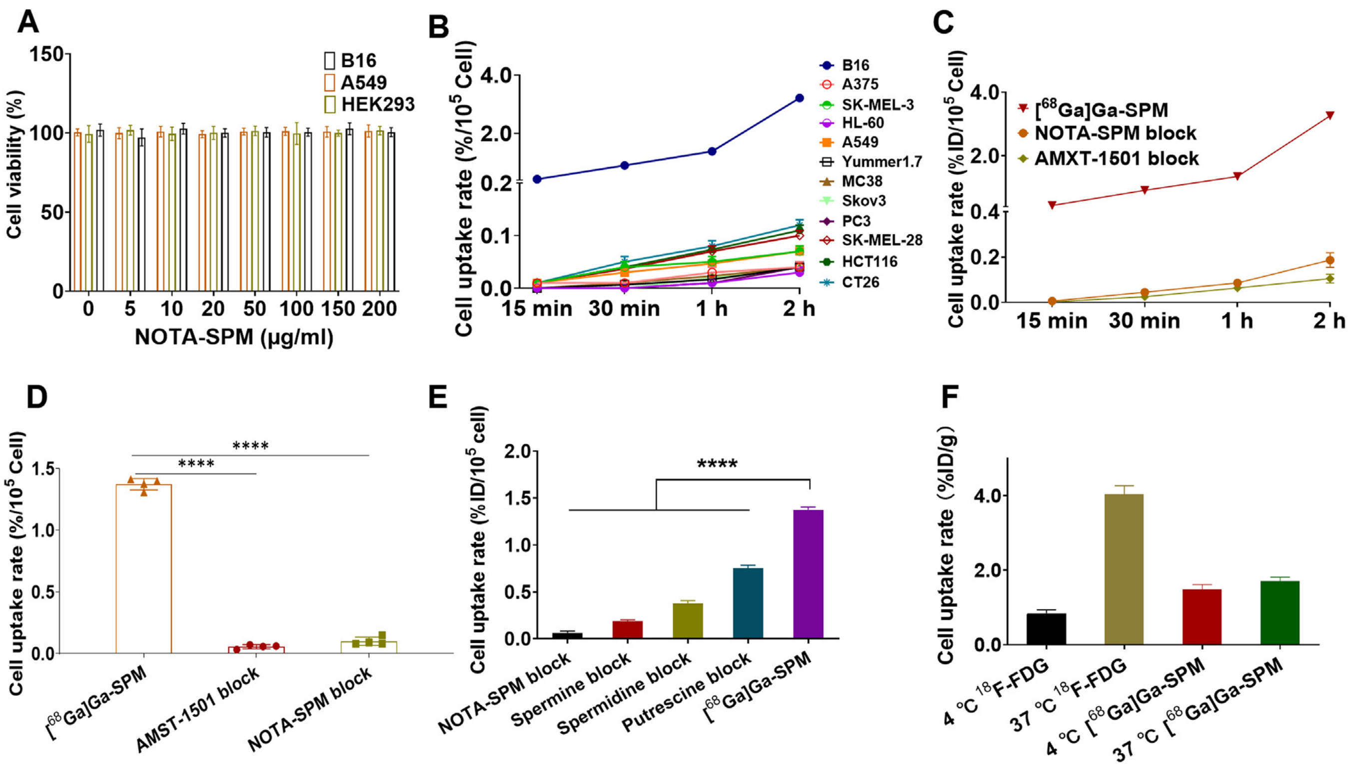

Fig. 2 – Cytotoxicity and cell uptake and blocking experiments. (A) Cell toxicity of NOTA-SPM incubated with B16, A549 B16 and HEK293 cells using the CCK-8 assay. No cytotoxicity was observed on all cells from NOTA-SPM itself. (B) Cell uptake of [^{68}Ga]Ga-SPM after incubation in 12 kinds of tumor cell lines for different time. (C) Cell uptake of [^{68}Ga]Ga-SPM after different time of incubation in B16 cell lines pretreated with NOTA-SPM and AMTX-1501 for blocking or inhibiting PTS, and (D) their quantitative results in 1 h. (E) Cell uptake of [^{68}Ga]Ga-SPM after 1 h of incubation in B16 cell lines pretreated with NOTA-SPM, spermine, spermidine and putrescine. (F) Uptake of [^{68}Ga]Ga-SPM and [^{18}F]FDG by B16 cell line at different culture temperatures. The data are shown as mean ± SD, ****P < 0.0001.

to C57BL/6 mice and collected urine and blood samples after a 30-min interval. Following purification with acetonitrile, HPLC analysis underscored the robust stability of [^{68}Ga]Ga-SPM, revealing radiochemical purities exceeding 90% in both blood and urine samples (Fig. 1D). This underscores the ability of [^{68}Ga]Ga-SPM to maintain excellent stability within both *in vitro* and *in vivo* metabolic environments. Furthermore, the partition coefficient of [^{68}Ga]Ga-SPM in a lipid-water system at pH 7.4 was determined, yielding a LogD value of -3.7 ± 0.44, along with a molar activity of $270.1 \pm 11.3 \times 10^3$ GBq/mmol. These values collectively attest to the high water solubility and specific activity of [^{68}Ga]Ga-SPM. Subsequently, the pharmacokinetics of [^{68}Ga]Ga-SPM was performed in C57BL/6 mice with the half-life of 16.2 min (Fig. S5). Collectively, [^{68}Ga]Ga-SPM emerges as a highly promising PET molecular probe. It offers the advantages of facile synthesis, a notable radiolabeling yield, exceptional radiochemical purity, robust stability, and a commendable specific activity.

3.2. *PTS-mediated recognition of [^{68}Ga]Ga-SPM by tumor cells in vitro*

After conducting a comprehensive structural characterization, we delved into the biomedical implications of [^{68}Ga]Ga-SPM. In the context of its potential biomedical applications, ensuring its safety is paramount. To assess this, we conducted CCK-8 assays on A549 and B16 tumor cells as well as HEK293 human embryonic kidney cells using the non-radioactive precursor NOTA-SPM of [^{68}Ga]Ga-SPM. Our results demonstrated that even at a concentration as high as 200 μg/ml (millimolar level), NOTA-SPM exhibited negligible toxicity towards all cell lines (Fig. 2A). Given that the dosage range for [^{68}Ga]Ga-SPM PET/CT imaging in humans falls within the nanomolar range, these findings substantiate the non-toxic nature of NOTA-SPM and its suitability for human applications. What's more, we also researched the anti-tumor effects of [^{177}Lu]Lu-SPM in B16 cells *in vitro* and the result showed significant differences among the blank control group, 0.185 MBq, 0.37 MBq, and 0.74 MBq nuclide treatment groups (P<0.0001, n = 5), indicating that [^{177}Lu]Lu-SPM has a significant killing effect on tumor cells *in vitro* (Fig. S6).

Subsequently, we conducted uptake experiments with [^{68}Ga]Ga-SPM across 12 distinct tumor cell lines. Intriguingly, most of these tumor cell lines exhibited minimal uptake of [^{68}Ga]Ga-SPM, with cellular uptake rates < 0.12%/10^5 cells after 2 h (Fig. 2B). This observation diverges from the findings reported by Allen et al. [45–47], where HCT116 and A549 cells displayed substantial uptake of spermine derivatives. We

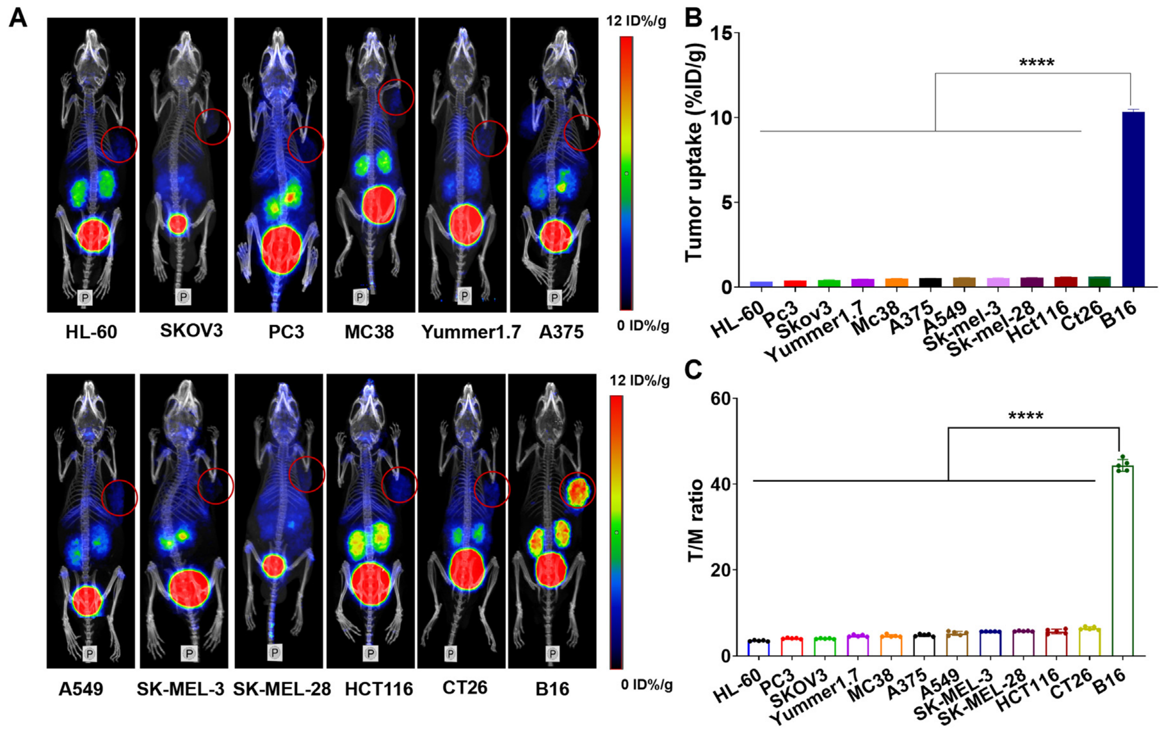

Fig. 3 – [^{68}Ga]Ga-SPM PET/CT imaging in 12 kinds of tumor models after injection of approximately 5.55 MBq (140 µl, 0.10 nmol) of [^{68}Ga]Ga-SPM. (A) [^{68}Ga]Ga-SPM PET/CT imaging of different tumor models. (B) Tumor uptakes of [^{68}Ga]Ga-SPM were derived from PET images and (C) their T/M ratio. The data are shown as mean ± SD, ****P < 0.0001.

attribute this discrepancy to the markedly higher doses of spermine derivatives employed in their studies, which were intended for therapeutic purposes and were a thousandfold greater than our diagnostic doses. Notably, among the tested cell lines, only the B16 cell line demonstrated significant uptake of the probe, which increased over time, culminating in a 2-h uptake rate of 3.21 ± 0.11%/10^5 cells. This observation indirectly underscores the higher affinity of the B16 cell line for spermine derivatives.

In this study, our probe was designed to target tumor cells through its interaction with the PTS. To substantiate this mechanism, we conducted blocking experiments in the B16 cell line using the non-radioactive precursor NOTA-SPM and the PTS inhibitor AMXT-1501. Specifically, NOTA-SPM primarily reduced the uptake of [^{68}Ga]Ga-SPM by B16 cells through competitive inhibition, while AMXT-1501 inhibited the activity of PTS, consequently diminishing its uptake of polyamines/polyamine derivatives. As anticipated, both pretreatments significantly curtailed the uptake of [^{68}Ga]Ga-SPM by B16 cells across all time points, exhibiting a more than tenfold difference in uptake rate at 2 h (Fig. 2C and D). These findings align with the use of spermine analogs in pancreatic cancer therapy [48] and PTS inhibitors in glioma treatment [49], providing compelling evidence for the PTS-mediated recognition of tumor cells by [^{68}Ga]Ga-SPM. To further validate this mechanism, we conducted blocking experiments with three distinct polyamines (spermine, spermidine, and putrescine). Encouragingly, all three substances substantially impeded the uptake of [^{68}Ga]Ga-SPM, with increasing blocking efficiency as their molecular structures progressively resembled that of [^{68}Ga]Ga-SPM (Fig. 2E, refer to their structural comparison in Fig. S3). This outcome underscores the differential affinities of PTS for these diverse polyamine substrates [50,51].

Notably, the prevailing PET/CT imaging agent in clinical practice, [^{18}F]FDG, is a radiolabeled glucose analog that enters cells via glucose transporters (GLUTs) through active receptor-mediated, energy-consuming processes [52]. To shed light on the PTS-mediated uptake mechanism of [^{68}Ga]Ga-SPM, we conducted uptake experiments at different temperatures, employing [^{18}F]FDG as a comparative reference. As anticipated, the uptake of [^{18}F]FDG by B16 cells exhibited a significant temperature dependency, with higher uptake observed at 37 °C compared to 4 °C (Fig. 2F). In contrast, the uptake of [^{68}Ga]Ga-SPM displayed no discernible temperature-related variations, indicating that the PTS-mediated uptake of [^{68}Ga]Ga-SPM is not solely energy-dependent. This finding contrasts with the hypothesis proposed by Grillo et al. [53]. In light of these observations, we posit that PTS-mediated cellular internalization of polyamines follows a passive binding and diffusion process rather than an actively energy-driven mechanism.

3.3. *PET/CT tumor imaging and biodistribution of [^{68}Ga]Ga-SPM in vivo*

The above experiments have convincingly established the specificity of [^{68}Ga]Ga-SPM for B16 cells among the diverse array of 12 tumor cell lines, thereby underscoring its potential utility in the diagnosis and treatment of melanoma. To

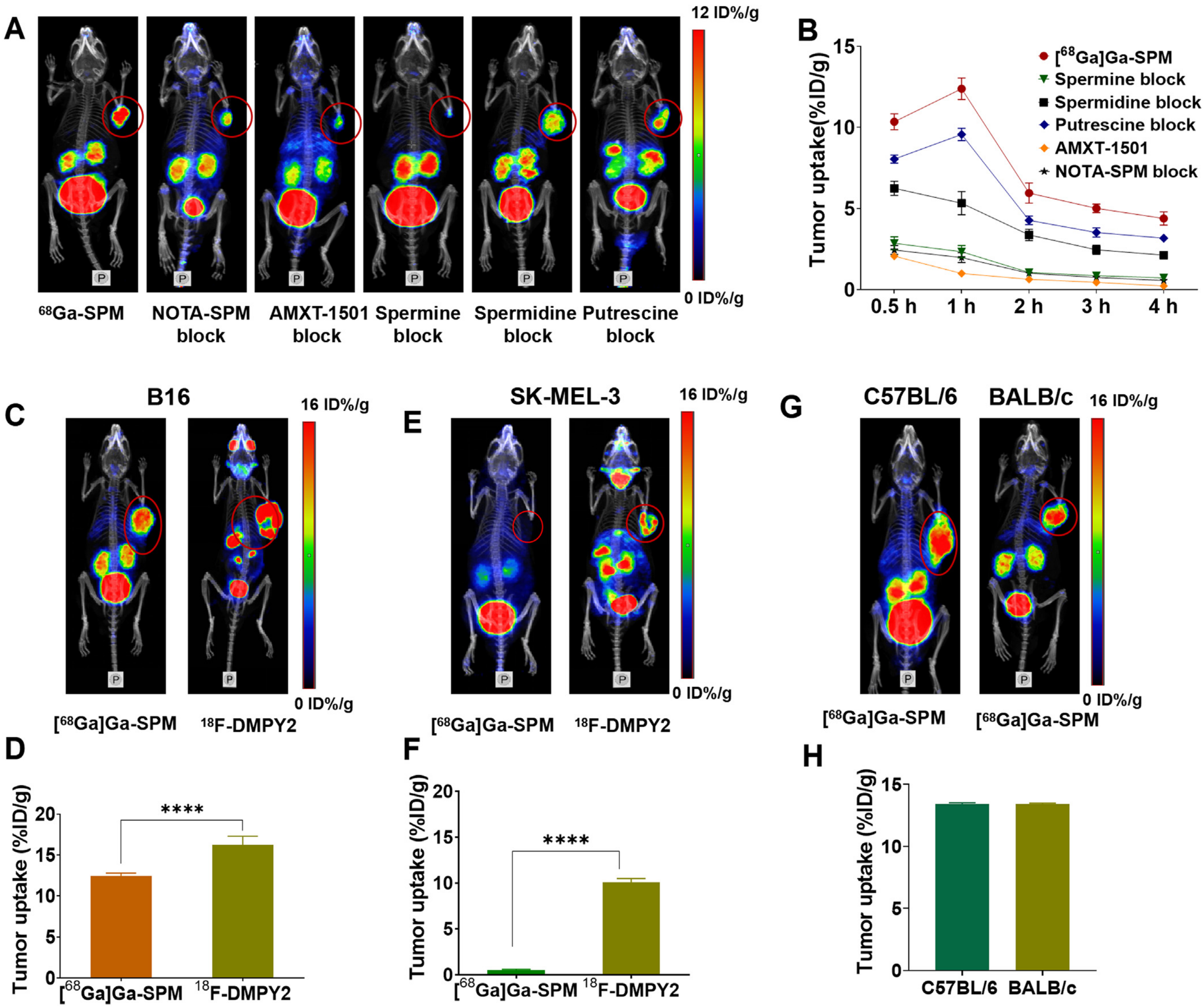

Fig. 4 – *In vivo* PET imaging: (A) [^{68}Ga]Ga-SPM PET/CT imaging in B16 tumor models with or without pretreatment with NOTA-SPM, AMTX-1501, spermine, spermidine or putrescine and (B) their tumor uptake of [^{68}Ga]Ga-SPM derived from corresponding dynamic PET images. (C) PET/CT imaging of [^{68}Ga]Ga-SPM and [^{18}F]DMPY2 in B16 and (D) its tumor uptakes derived from PET images. (E) PET/CT imaging of [^{68}Ga]Ga-SPM and [^{18}F]DMPY2 in SK-MEL-3 and (F) its tumor uptakes derived from PET images. (G) PET/CT imaging of [^{68}Ga]Ga-SPM in C57BL/ 6 with B16 tumor and BALB/c with B16 and (H) their tumor uptakes of [^{68}Ga]Ga-SPM. The data are shown as mean ± SD, ****$P < 0.0001$.

substantiate this observation, we embarked on *in vivo* imaging studies, employing tumor-bearing mouse models. Static PET/CT imaging outcomes across the 12 distinct tumor models consistently mirrored the cellular uptake findings, where [^{68}Ga]Ga-SPM exhibited pronounced accumulation in B16 tumors, while negligible accumulation was evident in the remaining 11 tumor types (Fig. 3A). Importantly, the imaging agent exhibited rapid clearance from non-target organs such as blood, brain, liver, and muscle, with subsequent excretion via the urinary system. This dynamic resulted in a substantial accumulation of [^{68}Ga]Ga-SPM in the kidneys and bladder. The uptake of [^{68}Ga]Ga-SPM by B16 tumors reached 10.33 ± 0.16 %ID/g just 0.5 h post-injection, with a tumor-to-muscle (T/M) ratio of 44.40 ± 1.38. In stark contrast, the uptake of [^{68}Ga]Ga-SPM by other tumors failed to surpass 1.0 %ID/g, yielding T/M ratios of less than 7.0 (Fig. 3B and C).

The biodistribution profiles of [^{68}Ga]Ga-SPM in tumor-bearing mice were in alignment with the PET/CT imaging findings, reflecting rapid and widespread distribution in various tissue organs. However, it was notable that [^{68}Ga]Ga-SPM exhibited swift clearance from non-target organs, with pronounced retention in tumor tissue and significant accumulation exclusively in the excretory organ, the kidney. Notably, 1 h post-injection of the imaging agent, tumor uptake reached its zenith at 9.33 ± 0.61 %ID/g. Importantly, this uptake was effectively attenuated by pre-administration of the non-radioactive precursor NOTA-SPM, resulting in a substantial reduction in uptake values to 2.14 ± 0.28 %ID/g

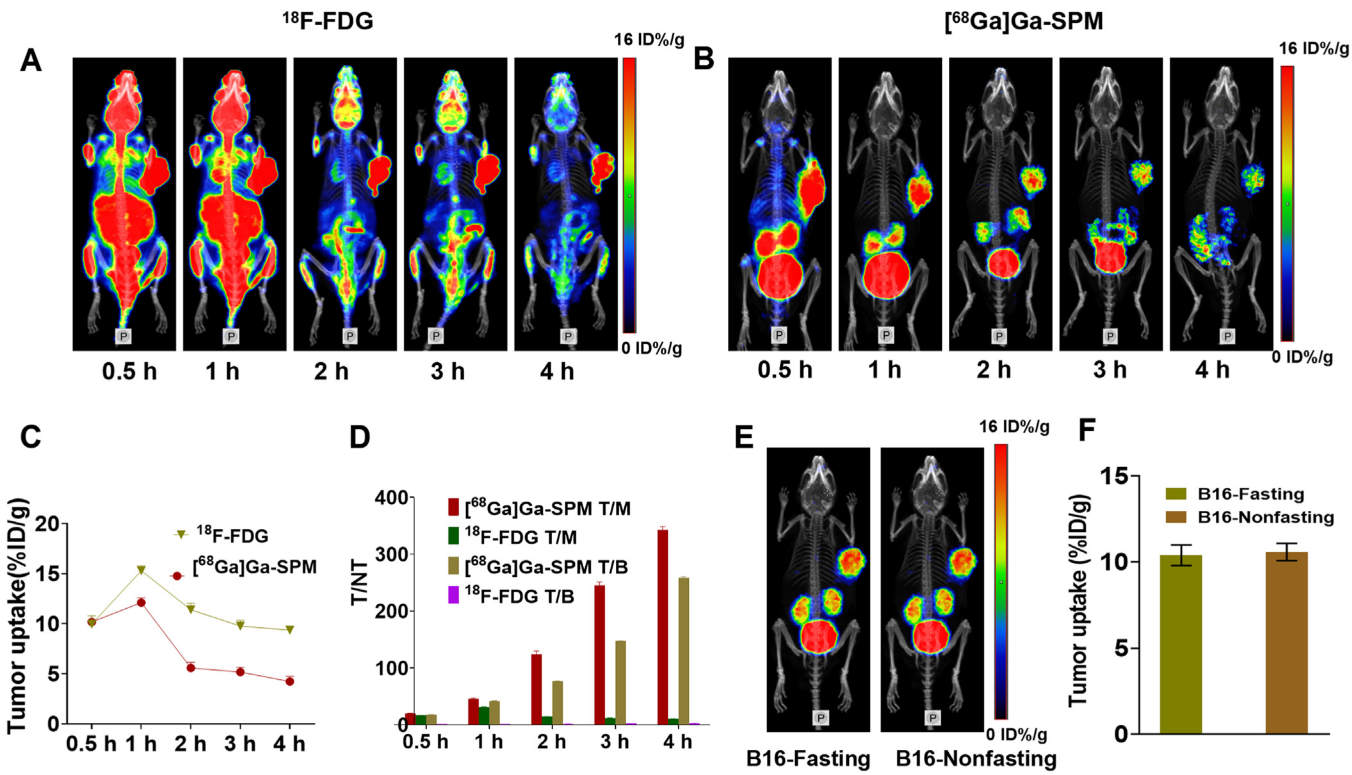

Fig. 5 – Head-to-head comparisons of [^{68}Ga]Ga-SPM and [^{18}F]FDG PET/CT in B16 models. (A) Dynamic [^{18}F]FDG and (B) [^{68}Ga]Ga-SPM PET/CT imaging for 4 h in B16 models. (C) Tumor uptake and (D) tumor to non-tumor ratio (T/NT) of [^{68}Ga]Ga-SPM and [^{18}F]FDG derived from corresponding dynamic PET/CT images. (E) [^{68}Ga]Ga-SPM PET/CT imaging in B16 with or without fasting and (F) its tumor uptakes derived from PET/CT images. The data are shown as mean ± SD.

($P < 0.0001$), while concomitantly, there was a modest elevation in the concentration of the imaging agent within the bloodstream and urinary system (Fig. S7).

3.4. *Confirmation of the tumor targeting mechanism of [^{68}Ga]Ga-SPM in vivo*

To further elucidate the *in vivo* tumor targeting mechanism of [^{68}Ga]Ga-SPM, we conducted blocking imaging experiments at the animal level. These experiments employed AMXT-1501, the non-radioactive precursor NOTA-SPM, and an excess of three polyamine substances. The results indicated that the AMXT-1501 group exhibited the most effective blocking, followed by the precursor NOTA-SPM group, spermine group, spermidine group, and putrescine group (Fig. 4A and B). These observations were consistent with the blocking outcomes at the cellular level. At the peak uptake time of 1 h, the uptake values of the imaging agent in the tumors of the [^{68}Ga]Ga-SPM group, AMXT-1501 group, precursor group, and spermine, spermidine, and putrescine groups were as follows: 12.38 ± 0.67 %ID/g, 1.00 ± 0.07 %ID/g, 1.98 ± 0.31 %ID/g, 2.34 ± 0.38 %ID/g, 5.33 ± 0.72 %ID/g, and 9.57 ± 0.38 %ID/g, respectively (Fig. 4B). The dynamic imaging and T/M results are presented in Figs. S8 and S9. This animal-level verification once again corroborated that the targeting specificity of [^{68}Ga]Ga-SPM is achieved through PTS-mediated binding.

Given that B16 was the sole tumor model among the 12 tested that exhibited a robust response to [^{68}Ga]Ga-SPM, it is plausible that this result may be linked to melanin content. Therefore, we conducted *in vivo* imaging experiments employing mouse-derived melanoma B16 and human-derived melanoma SK-MEL-3 models. In these experiments, we utilized the melanin-targeting probe [^{18}F]DMPY2 PET/CT as a control [54]. Notably, [^{18}F]DMPY2 exhibited significant signals in both melanin-producing B16 and SK-MEL-3 tumors (Fig. 4C–F). In contrast, [^{68}Ga]Ga-SPM was notably taken up only by B16 tumors and not by SK-MEL-3 tumors. This outcome effectively refutes the hypothesis that the imaging principle of [^{68}Ga]Ga-SPM in B16 tumors is melanin-related.

Emerging evidence suggests that higher polyamine levels in tumors are associated with the immunosuppressive properties commonly observed in malignant tumors [34,55]. To investigate whether variations exist in the uptake of [^{68}Ga]Ga-SPM by B16 tumors in different immune microenvironments, we separately implanted B16 cells into C57BL/6 mice and BALB/c mice and subsequently performed [^{68}Ga]Ga-SPM PET/CT imaging on both groups after tumor formation. The results unveiled favorable imaging outcomes in both settings, with B16 tumors exhibiting significant uptake of [^{68}Ga]Ga-SPM without substantial differences between the immune environments (Fig. 4G and H). This observation implies that [^{68}Ga]Ga-SPM is primarily taken

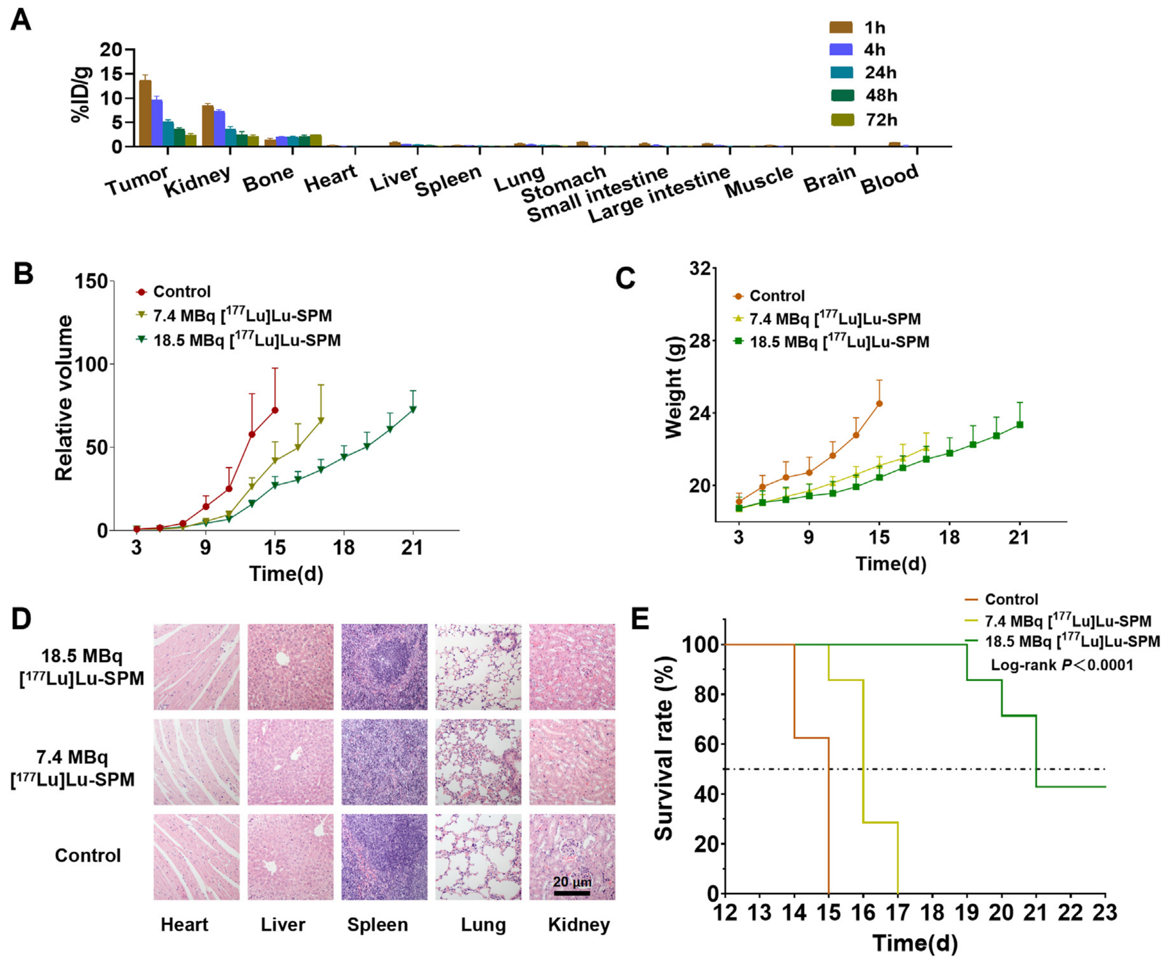

Fig. 6 – Therapy and efficacy assessment of [^{177}Lu]Lu-SPM on B16 tumor. (A) Biodistribution of [^{177}Lu]Lu-SPM in B16 models. The accumulation of [^{177}Lu]Lu-SPM (%ID/g) in tumors and normal organs at different time points was demonstrated. (B) Tumor growth curves relative to the tumor volume at Day 3 (set as 1.0) for mice among the 3 groups. (C) The weight of mice among the 3 groups. (D) HE staining of heart, liver, spleen, lung and kidney tissue sections of 3 groups. (E) Kaplan-Meier plot of 3 groups. The data are shown as mean ± SD.

up by tumor cells and remains unaffected by the tumor microenvironment.

3.5. A comparison of [^{68}Ga]Ga-SPM with [^{18}F]FDG for PET/CT tumor imaging

In light of the remarkable imaging performance of [^{68}Ga]Ga-SPM in B16 tumors, we sought to ascertain whether its imaging capabilities could rival those of [^{18}F]FDG, a widely recognized PET/CT imaging gold standard. Both [^{68}Ga]Ga-SPM and [^{18}F]FDG distinctly depicted B16 tumors (Fig. 5A–D). Both imaging agents provided clear tumor visualization at 0.5 h post-injection, with optimal results and peak uptake observed at the 1-h mark (12.38 ± 0.67 %ID/g for [^{68}Ga]Ga-SPM *vs* 15.61 ± 1.69 for [^{18}F]FDG). Notably, the T/M and tumor-to-brain ratio (T/B) reached their zenith at 1 h post-probe injection, followed by a gradual decline. While B16 displayed a higher specific uptake of [^{18}F]FDG compared to [^{68}Ga]Ga-SPM, it is noteworthy that [^{18}F]FDG also exhibited significantly greater accumulation in non-target organs such as the heart, brain, liver, and intestines when compared to [^{68}Ga]Ga-SPM. The T/M and T/B values for tumors in [^{68}Ga]Ga-SPM imaging gradually increased over time and were markedly superior to those of [^{18}F]FDG. Specifically, at the 4-h mark, the T/M and T/B values for tumors were 344.2 ± 1.93 and 258.19 ± 2.3 for [^{68}Ga]Ga-SPM, in contrast to 10.71 ± 0.36 and 2.77 ± 0.05 for [^{18}F]FDG. It is pertinent to mention that both our study and the findings of Volkow et al. [56]. underscore the inability of radiolabeled polyamines to penetrate the normal blood–brain barrier.

Additionally, we conducted a comparative assessment of PET/CT imaging with [^{68}Ga]Ga-SPM in B16 tumor-bearing mice under fasting and non-fasting conditions. Intriguingly, imaging under non-fasting conditions yielded results on par with those obtained under fasting conditions, with no discernible disparity between the two (Fig. 5E and F). In contrast, PET/CT imaging with [^{18}F]FDG necessitates a fasting period of at least 4–6 h, coupled with the imperative control of blood glucose levels below 10 mmol/l to avoid compromising imaging efficacy [57]. In summary, [^{68}Ga]Ga-SPM holds the potential to replace [^{18}F]FDG entirely in B16 tumor imaging,

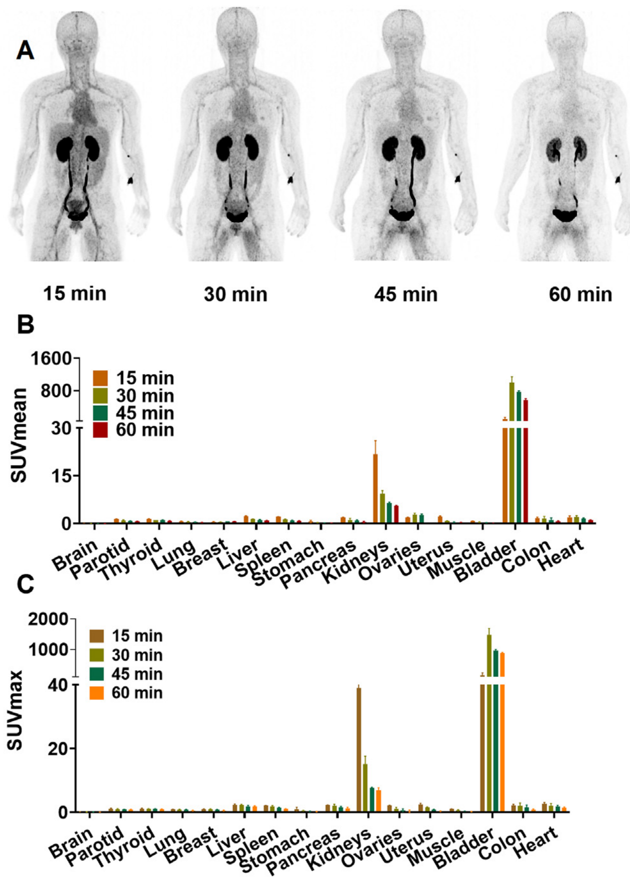

D

Target Organ	Organ Doses (mSv/MBq)	
	Mean	SD
Adrenals	1.53E-02	1.57E-03
Brain	2.47E-03	2.10E-04
Breasts	5.61E-03	3.99E-04
Esophagus	1.54E-02	1.26E-03
Eyes	1.45E-02	1.26E-03
Gallbladder Wall	1.71E-02	1.46E-03
Left colon	1.70E-02	1.45E-03
Small Intestine	1.22E-02	4.41E-03
Stomach Wall	1.81E-02	1.46E-03
Right colon	7.28E-03	6.16E-04
Rectum	9.85E-03	8.48E-04
Heart Wall	1.08E-02	9.18E-04
Kidneys	4.82E-02	1.48E-03
Liver	7.34E-03	6.60E-04
Lungs	1.80E-02	1.51E-03
Ovaries	1.38E-02	9.91E-04
Pancreas	1.80E-02	1.45E-03
Salivary Glands	9.86E-03	1.20E-03
Red Marrow	1.70E-02	1.45E-03
Osteogenic Cells	1.05E-02	9.59E-04
Spleen	1.76E-02	1.27E-03
Thymus	1.64E-02	1.40E-03
Thyroid	1.58E-02	1.29E-03
Urinary Bladder Wall	2.63E-02	1.33E-03
Uterus	1.53E-02	1.36E-03
Total Body	1.61E-02	1.39E-03
Effective Dose(mSv/MBq)	1.78E-02	7.21E-04

Fig. 7 – [^{68}Ga]Ga-SPM PET imaging in healthy volunteers (n = 3). (A) Maximum intensity projection imaging at different time points after injection. The SUV_{mean} (B) and SUV_{max} (C) value of normal organ uptake of [^{68}Ga]Ga-SPM. The data are shown as mean ± SD. (D) Human organ radiation dosimetry estimates for [^{68}Ga]Ga-SPM.

particularly in scenarios involving diabetic patients and presentations involving brain metastases, where it may offer distinct advantages.

3.6. Anti-tumor therapeutic application of [^{177}Lu]Lu-SPM in vivo

Malignant melanoma, recognized as the most aggressive and lethal skin cancer, has exhibited an alarming rise in global incidence [2]. Current therapeutic approaches for melanoma predominantly encompass surgery, chemotherapy, immunotherapy, and radiotherapy. However, metastatic melanoma often develops resistance to prevailing chemotherapy and immunotherapy regimens, resulting in an average survival duration of merely 3–15 months [58,59]. Consequently, there is an urgent need for effective interventions against advanced melanoma. In contrast to external radiation therapy and chemotherapy, targeted radiopharmaceutical therapy for melanoma offers the potential to selectively deliver radiation doses to tumor cells, thus minimizing damage to normal tissues. The preceding findings highlight the substantial uptake and favorable target-to-background ratio of [^{68}Ga]Ga-SPM in B16 tumors. Consequently, we conjectured that therapeutic nuclear-labeled SPM might hold promise as a melanoma treatment strategy. To validate this hypothesis, we employed a commonly used therapeutic nuclide [^{177}Lu] in clinical practice to label SPM. Notably, it displayed the highest accumulation in B16 tumor-bearing mice and exhibited prolonged retention, primarily in the kidneys, with minimal retention in most other tissue organs (Fig. 6A), consistent with the biodistribution patterns observed for [^{68}Ga]Ga-SPM. To evaluate the therapeutic potential of [^{177}Lu]Lu-SPM against B16 tumors, we randomly divided B16 tumor-bearing mice into three groups: a PBS blank control group, a 7.4 MBq [^{177}Lu]Lu-SPM nuclear therapy group, and an 18.5 MBq [^{177}Lu]Lu-SPM nuclear therapy group. At the outset of treatment, there were no discernible differences in body weight or tumor volume among the three groups (Figs. 6B and C, and S10). Subsequently, tumor size and weight progressively increased over time in the blank control group.

On the second day following the initial treatment, significant disparities in tumor size and weight emerged between the blank control group and the nuclear therapy groups ($P < 0.01$). Seven days after the second treatment, a marked discrepancy in B16 tumor volume was evident between the 7.4 MBq and 18.5 MBq [^{177}Lu]Lu-SPM nuclear therapy groups. Since the growth rate of B16 tumors in the blank control group was very fast, the body weight of mice with solid tumor weight was much higher than that of the nuclide treatment groups where tumor growth was suppressed. While, despite tumor growth, the body weight of mice in both nuclear therapy groups steadily increased, with no significant disparity between them, indicative of the absence of substantial adverse effects on the overall health of the mice. This observation was further corroborated by the histological analysis of heart, liver, spleen, lung, and kidney tissues, which exhibited no discernible differences among the three groups (Fig. 6D).

The ultimate therapeutic outcome was evaluated through the assessment of survival rates. The average survival time for mice in the blank control group was 14.63 ± 0.52 d. Following nuclear therapy, mice survival was significantly extended, reaching 16.14 ± 0.69 and 21.43 ± 1.72 d for the 7.4 MBq and 18.5 MBq [^{177}Lu]Lu-SPM nuclear therapy groups, respectively (Fig. 6E). This extension in survival exhibited a dose-dependent therapeutic efficacy. In comparison, our therapeutic effect surpassed that of targeted melanocortin-1 receptor (MC1-R)-specific [^{188}Re]Re-(Arg11)CCMSH [60], but was inferior to that of [^{212}Pb]Pb-DOTA-Re(Arg11)CCMSH [61], which emits α-rays. However, it is worth noting that [^{212}Pb]Pb-DOTA-Re(Arg11)CCMSH exhibited moderate kidney toxicity at a dose of 7.4 MBq, limiting its clinical applicability. As a radiopharmaceutical emitting medium-to-low-energy β-rays, [^{177}Lu]Lu is more suitable for the treatment of small tumors and metastases [62,63].

3.7. Human organ distribution and dosimetry of [^{68}Ga]Ga-SPM

In preparation for the prospective clinical translation of [^{68}Ga]Ga-SPM, it is imperative to ascertain the safety of intravenous administration of this radiopharmaceutical in humans. Accordingly, we conducted an initial safety assessment by investigating the distribution of the required dose of [^{68}Ga]Ga-SPM (3.7 MBq/kg) and the associated radiation dose in healthy volunteers. The outcomes of this study revealed that, aside from substantial accumulation in the urinary excretory system, [^{68}Ga]Ga-SPM exhibited rapid clearance from various other vital tissue organs, including the blood, heart, liver, spleen, lungs, and brain, with negligible background levels (Fig. 7A–C).

The radiation doses incurred by [^{68}Ga]Ga-SPM, as computed employing the OLINDA (Version 2.2) software, are presented in Fig. 7D. The kidneys, serving as the primary excretion organs for this radiopharmaceutical, registered the highest exposure dose at 4.82E-02 ± 1.48E-03 mSv/MBq, followed by the bladder wall at 2.63E-02 ± 1.33E-03 mSv/MBq. The overall effective dose to the whole body was calculated to be 1.78E-02 ± 7.21E-04 mSv/MBq, a value lower than that typically associated with the clinically routine PET/CT imaging agent [^{18}F]FDG [57]. Consequently, the usage of [^{68}Ga]Ga-SPM is considered to be highly safe for human applications. These findings establish a robust foundation for subsequent clinical translation endeavors.

4. Conclusion

In the pursuit of effective tools for tumor diagnosis and therapy, this study introduces [^{68}Ga]Ga-SPM, a novel PET probe targeting PTS. The probe showcases rapid synthesis, high purity, and exceptional stability, positioning it as a promising candidate for tumor imaging. Rigorous *in vitro* and *in vivo* investigations unequivocally confirm its specific uptake in melanoma cells, facilitated by PTS, highlighting its potential for precise tumor detection. [^{68}Ga]Ga-SPM primarily undergoes urinary excretion *in vivo*, exhibiting minimal uptake in normal tissues and organs, thereby yielding an impressive tumor-to-non-tumor ratio. Unlike the widely utilized [^{18}F]FDG, [^{68}Ga]Ga-SPM's uptake remains impervious to various influencing factors, enhancing its suitability for clinical application. Furthermore, [^{68}Ga]Ga-SPM successfully evolves into a therapeutic nuclear probe ([^{177}Lu]Lu-SPM), demonstrating substantial promise in restraining tumor growth. Human-level investigations corroborate its safety profile and low radiation exposure, thus setting the stage for clinical translation. In summation, [^{68}Ga]Ga-SPM emerges as a propitious PET probe capable of serving dual roles in accurate tumor diagnosis and polyamine-targeted cancer therapies, holding immense potential for enhancing patient outcomes in the ongoing battle against cancer. A compelling avenue for further exploration involves the identification of human-derived tumor cell lines with elevated PTS expression, potentially catalyzing direct clinical applications of SPM-based nuclear probes.

Conflicts of interest

The authors declare that they have no competing interests.

Acknowledgments

This work was supported by the Science and Technology Innovation Team Talent Project of Hunan Province (No.2021 RC4056), the clinical research foundation of the National Clinical Research Center for Geriatric Diseases (XIANGYA) (No.2020LNJJ01), the Natural Science Foundation of Hunan Province in China (No.2021JJ20084), and the Science and Technology Innovation Program of Hunan Province (No. 2021RC3020).

Supplementary materials

Supplementary material associated with this article can be found, in the online version, at doi:10.1016/j.ajps.2024.100924.

References

[1] Zheng R, Zhang S, Zeng H, Wang S, Sun K, Chen R, et al. Cancer incidence and mortality in China, 2016. J Natl Cancer Center 2022;2(1):1–9.
[2] Siegel RL, Miller KD, Fuchs HE, Jemal A. Cancer statistics, 2022. CA Cancer J Clin 2022;72(1):7–33.
[3] Gambhir SS. Molecular imaging of cancer with positron emission tomography. Nat Rev Cancer 2002;2(9):683–93.
[4] Basu S, Alavi A. Unparalleled contribution of 18F-FDG PET to medicine over 3 decades. J Nucl Med 2008;49(10) 17n–21n, 37n.

[5] Ni D, Ehlerding EB, Cai W. Multimodality imaging agents with PET as the fundamental pillar. Angew Chem Int Ed Engl 2019;58(9):2570–9.
[6] Shankar LK. The clinical evaluation of novel imaging methods for cancer management. Nat Rev Clin Oncol 2012;9(12):738–44.
[7] Kenny L, Coombes RC, Vigushin DM, Al-Nahhas A, Shousha S, Aboagye EO. Imaging early changes in proliferation at 1 week post chemotherapy: a pilot study in breast cancer patients with 3′-deoxy-3′-[18F]fluorothymidine positron emission tomography. Eur J Nucl Med Mol Imaging 2007;34(9):1339–47.
[8] Harris SM, Davis JC, Snyder SE, Butch ER, Vavere AL, Kocak M, et al. Evaluation of the biodistribution of 11C-methionine in children and young adults. J Nucl Med 2013;54(11):1902–8.
[9] Poulsen SH, Urup T, Grunnet K, Christensen IJ, Larsen VA, Jensen ML, et al. The prognostic value of FET PET at radiotherapy planning in newly diagnosed glioblastoma. Eur J Nucl Med Mol Imaging 2017;44(3):373–81.
[10] Unterrainer M, Schweisthal F, Suchorska B, Wenter V, Schmid-Tannwald C, Fendler WP, et al. Serial 18F-FET PET imaging of primarily 18F-FET-negative glioma: does it make sense? J Nucl Med 2016;57(8):1177–82.
[11] Evangelista L, Guttilla A, Zattoni F, Muzzio PC, Zattoni F. Utility of choline positron emission tomography/computed tomography for lymph node involvement identification in intermediate- to high-risk prostate cancer: a systematic literature review and meta-analysis. Eur Urol 2013;63(6):1040–8.
[12] Kelloff GJ, Hoffman JM, Johnson B, Scher HI, Siegel BA, Cheng EY, et al. Progress and promise of FDG-PET imaging for cancer patient management and oncologic drug development. Clin Cancer Res 2005;11(8):2785–808.
[13] Ning X, Seo W, Lee S, Takemiya K, Rafi M, Feng X, et al. PET imaging of bacterial infections with fluorine-18-labeled maltohexaose. Angew Chem Int Ed Engl 2014 15;53(51):14096–101.
[14] Shreve PD, Anzai Y, Wahl RL. Pitfalls in oncologic diagnosis with FDG PET imaging: physiologic and benign variants. Radiographics 1999;19(1):61–77 quiz 150-1.
[15] Hellwig D, Graeter TP, Ukena D, Groeschel A, Sybrecht GW, Schaefers HJ, et al. 18F-FDG PET for mediastinal staging of lung cancer: which SUV threshold makes sense? J Nucl Med 2007;48(11):1761–6.
[16] Boellaard R, Oyen WJ, Hoekstra CJ, Hoekstra OS, Visser EP, Willemsen AT, et al. The Netherlands protocol for standardisation and quantification of FDG whole body PET studies in multi-centre trials. Eur J Nucl Med Mol Imaging 2008;35(12):2320–33.
[17] Lindholm P, Minn H, Leskinen-Kallio S, Bergman J, Ruotsalainen U, Joensuu H. Influence of the blood glucose concentration on FDG uptake in cancer–a PET study. J Nucl Med 1993;34(1):1–6.
[18] Vriens D, Visser EP, de Geus-Oei LF, Oyen WJ. Methodological considerations in quantification of oncological FDG PET studies. Eur J Nucl Med Mol Imaging 2010;37(7):1408–25.
[19] van Marken Lichtenbelt WD, Vanhommerig JW, Smulders NM, Drossaerts JM, Kemerink GJ, Bouvy ND, et al. Cold-activated brown adipose tissue in healthy men. N Engl J Med 2009;360(15):1500–8.
[20] Pegg AE, Casero RA Jr. Current status of the polyamine research field. Methods Mol Biol 2011;720:3–35.
[21] Terui Y, Yoshida T, Sakamoto A, Saito D, Oshima T, Kawazoe M, et al. Polyamines protect nucleic acids against depurination. Int J Biochem Cell Biol 2018;99:147–53.
[22] Kurata HT, Akrouh A, Li JB, Marton LJ, Nichols CG. Scanning the topography of polyamine blocker binding in an inwardly rectifying potassium channel. J Biol Chem 2013;288(9):6591–601.
[23] Rao JN, Rathor N, Zhuang R, Zou T, Liu L, Xiao L, et al. Polyamines regulate intestinal epithelial restitution through TRPC1-mediated Ca^{2}+ signaling by differentially modulating STIM1 and STIM2. Am J Physiol Cell Physiol 2012;303(3):C308–17.
[24] Uchida H, Itaka K, Uchida S, Ishii T, Suma T, Miyata K, et al. Synthetic polyamines to regulate mRNA translation through the preservative binding of eukaryotic initiation factor 4E to the cap structure. J Am Chem Soc 2016;138(5):1478–81.
[25] Nahi O, Kulak AN, Zhang S, He X, Aslam Z, Ilett MA, et al. Polyamines promote aragonite nucleation and generate biomimetic structures. Adv Sci (Weinh) 2022;10(1):e2203759.
[26] Gerner EW, Meyskens FL Jr. Polyamines and cancer: old molecules, new understanding. Nat Rev Cancer 2004;4(10):781–92.
[27] Lee MS, Dennis C, Naqvi I, Dailey L, Lorzadeh A, Ye G, et al. Ornithine aminotransferase supports polyamine synthesis in pancreatic cancer. Nature 2023;616(7956):339–47.
[28] Bello-Fernandez C, Packham G, Cleveland JL. The ornithine decarboxylase gene is a transcriptional target of c-Myc. Proc Natl Acad Sci USA 1993;90(16):7804–8.
[29] Origanti S, Shantz LM. Ras transformation of RIE-1 cells activates cap-independent translation of ornithine decarboxylase: regulation by the Raf/MEK/ERK and phosphatidylinositol 3-kinase pathways. Cancer Res 2007;67(10):4834–42.
[30] Chang BK, Libby PR, Bergeron RJ, Porter CW. Modulation of polyamine biosynthesis and transport by oncogene transfection. Biochem Biophys Res Commun 1988 30;157(1):264–70.
[31] Peters MC, Minton A, Phanstiel IO, Gilmour SK. A novel polyamine-targeted therapy for BRAF mutant melanoma tumors. Med Sci (Basel) 2018;6(1):3.
[32] Casero RA Jr, Murray ST, Pegg AE. Polyamine metabolism and cancer: treatments, challenges and opportunities. Nat Rev Cancer 2018;18(11):681–95.
[33] Alexander ET, Mariner K, Donnelly J, Phanstiel Ot, Gilmour SK. Polyamine blocking therapy decreases survival of tumor-infiltrating immunosuppressive myeloid cells and enhances the antitumor efficacy of PD-1 blockade. Mol Cancer Ther 2020;19(10):2012–22.
[34] Alexander ET, Minton A, Peters MC, Phanstiel Ot, Gilmour SK. A novel polyamine blockade therapy activates an anti-tumor immune response. Oncotarget 2017 13;8(48):84140–52.
[35] Levin VA, Ictech SE, Hess KR. Clinical importance of eflornithine (α-difluoromethylornithine) for the treatment of malignant gliomas. CNS Oncol 2018;7(2):Cns16.
[36] Ask A, Persson L, Heby O. Increased survival of L1210 leukemic mice by prevention of the utilization of extracellular polyamines. Studies using a polyamine-uptake mutant, antibiotics and a polyamine-deficient diet. Cancer Lett 1992;66(1):29–34.
[37] Gitto SB, Pandey V, Oyer JL, Copik AJ, Hogan FC, Phanstiel Ot, et al. Difluoromethylornithine combined with a polyamine transport inhibitor is effective against gemcitabine resistant pancreatic cancer. Mol Pharm 2018;15(2):369–76.
[38] Muth A, Madan M, Archer JJ, Ocampo N, Rodriguez L, Phanstiel Ot. Polyamine transport inhibitors: design, synthesis, and combination therapies with difluoromethylornithine. J Med Chem 2014;57(2):348–63.
[39] Dryja P, Fisher C, Woster PM, Bartee E. Inhibition of Polyamine biosynthesis using difluoromethylornithine acts as a potent immune modulator and displays therapeutic synergy with PD-1-blockade. J Immunother 2021;44(8):283–91.
[40] Soulet D, Gagnon B, Rivest S, Audette M, Poulin R. A fluorescent probe of polyamine transport accumulates into intracellular acidic vesicles via a two-step mechanism. J Biol Chem 2004;279(47):49355–66.

[41] Belting M, Mani K, Jönsson M, Cheng F, Sandgren S, Jonsson S, et al. Glypican-1 is a vehicle for polyamine uptake in mammalian cells: a pivital role for nitrosothiol-derived nitric oxide. J Biol Chem 2003;278(47):47181–9.
[42] Uemura T, Stringer DE, Blohm-Mangone KA, Gerner EW. Polyamine transport is mediated by both endocytic and solute carrier transport mechanisms in the gastrointestinal tract. Am J Physiol Gastrointest Liver Physiol 2010;299(2): G517–G522.
[43] Brink I, Hoegerle S, Klisch J, Bley TA. Imaging of pheochromocytoma and paraganglioma. Fam Cancer 2005;4(1):61–8.
[44] Pyo A, Kim DY, Kim H, Lim D, Kwon SY, Kang SR, et al. Ultrasensitive detection of malignant melanoma using PET molecular imaging probes. Proc Natl Acad Sci USA 2020;117(23):12991–9.
[45] Allen WL, McLean EG, Boyer J, McCulla A, Wilson PM, Coyle V, et al. The role of spermidine/spermineN1-acetyltransferase in determining response to chemotherapeutic agents in colorectal cancer cells. Mol. Cancer Ther. 2007;6(1): 128–137.
[46] Hacker A, Marton LJ, Sobolewski M, Casero RA. *In vitro* and *in vivo* effects of the conformationally restricted polyamine analogue CGC-11047 on small cell and non-small cell lung cancer cells. Cancer Chemother. Pharmacol. 2008;63(1):45–53.
[47] Kruczynski A, Vandenberghe I, Pillon A, Pesnel S, Goetsch L, Barret JM, et al. Preclinical activity of F14512, designed to target tumors expressing an active polyamine transport system. Invest New Drugs 2009;29(1):9–21.
[48] Bergeron RJ, Müller R, Bussenius J, McManis JS, Merriman RL, Smith RE, et al. Synthesis and evaluation of hydroxylated polyamine analogues as antiproliferatives. J Med Chem 2000;43(2):224–35.
[49] Khan A, Gamble LD, Upton DH, Ung C, Yu DMT, Ehteda A, et al. Dual targeting of polyamine synthesis and uptake in diffuse intrinsic pontine gliomas. Nat Commun 2021;12(1):971.
[50] Kumagai J, Jain R, Johnson LR. Characteristics of spermidine uptake by isolated rat enterocytes. Am J Physiol 1989;256(5):G905–10 Pt 1.
[51] De Smedt H, Van den Bosch L, Geuns J, Borghgraef R. Polyamine transport systems in the LLC-PK1 renal epithelial established cell line. Biochim Biophys Acta 1989;1012(2):171–7.
[52] Avril N. GLUT1 expression in tissue and (18)F-FDG uptake. J Nucl Med 2004;45(6):930–2.
[53] Grillo MA, Colombatto S. Polyamine transport in cells. Biochem Soc Trans 1994;22(4):894–8.
[54] Pyo A, Kim DY, Kim H, Lim D, Kwon SY, Kang SR, et al. Ultrasensitive detection of malignant melanoma using PET molecular imaging probes. Proc Natl Acad Sci 2020;117(23):12991–9.
[55] Hayes CS, Shicora AC, Keough MP, Snook AE, Burns MR, Gilmour SK. Polyamine-blocking therapy reverses immunosuppression in the tumor microenvironment. Cancer Immunol Res 2014;2(3):274–85.
[56] Volkow N, Goldman SS, Flamm ES, Cravioto H, Wolf AP, Brodie JD. Labeled putrescine as a probe in brain tumors. Science 1983;221(4611):673–5.
[57] Delbeke D, Coleman RE, Guiberteau MJ, Brown ML, Royal HD, Siegel BA, et al. Procedure guideline for tumor imaging with 18F-FDG PET/CT 1.0. J Nucl Med 2006;47(5):885–95.
[58] Balch CM, Soong SJ, Gershenwald JE, Thompson JF, Reintgen DS, Cascinelli N, et al. Prognostic factors analysis of 17,600 melanoma patients: validation of the American Joint Committee on Cancer melanoma staging system. J Clin Oncol 2001;19(16):3622–34.
[59] Anderson CM, Buzaid AC, Legha SS. Systemic treatments for advanced cutaneous melanoma. Oncology (Williston Park) 1995;9(11):1149–58 discussion 63-4, 67-8.
[60] Miao Y, Owen NK, Whitener D, Gallazzi F, Hoffman TJ, Quinn TP. *In vivo* evaluation of 188Re-labeled alpha-melanocyte stimulating hormone peptide analogs for melanoma therapy. Int J Cancer 2002;101(5):480–7.
[61] Miao Y, Hylarides M, Fisher DR, Shelton T, Moore H, Wester DW, et al. Melanoma therapy via peptide-targeted {alpha}-radiation. Clin Cancer Res 2005;11(15):5616–21.
[62] de Jong M, Breeman WA, Bernard BF, Bakker WH, Schaar M, van Gameren A, et al. [177Lu-DOTA(0),Tyr3] octreotate for somatostatin receptor-targeted radionuclide therapy. Int J Cancer 2001;92(5):628–33.
[63] Hoefnagel CA. Radionuclide therapy revisited. Eur J Nucl Med 1991;18(6):408–31.